AIAA JOURNAL
Vol. 30, No. 7, July 1992

Viscous High-Speed Flow Computations by Adaptive Mesh Embedding Techniques

F. Grasso,* M. Marini,† and M. Passalacqua†
Università di Roma "La Sapienza," 00184 Rome, Italy

In the present work, an adaptive mesh embedding technique has been developed for the solution of viscous high Mach number flows. The equations solved are the two-dimensional full Navier Stokes equations. A Runge Kutta finite volume formulation is used with symmetric discretization of both inviscid and viscous fluxes, and adaptive dissipation. The technique has been applied to a shock-wave boundary-layer laminar interaction problem and to a variety of flows over a (double ellipse) blunt body to study the effects of grid quality and topology of the adopted region on the solution accuracy. Computed results indicate that the selection of the most appropriate criterion for adaptation depends upon the physical phenomena of interest.

Introduction

THE development of high-speed maneuverable re-entry vehicles has refocused attention on the problem of accurately predicting flow features such as shock waves and their interactions with boundary layers.[1] These phenomena are rather localized and require accurate schemes and/or high mesh refinement in small portions of the computational domain.

During the last years, several upwind total variation diminishing (TVD) methods have been developed that give sharp representation of flow discontinuities, without using artificial dissipative terms.[2-5] In the recent past, numerical techniques for unstructured meshes have also received strong impulse for computational fluid dynamics (CFD) applications: unstructured grids allow grid points to concentrate where needed without introducing complications in the solution algorithm.[4] However, codes for unstructured meshes and/or based on TVD schemes are computationally expensive.

At present, adaptive mesh embedding on structured grids can be considered as an alternative and valuable tool to enhance, locally, the accuracy of numerical solutions, without excessive computational overhead.[5-10]

In the present work, adaptive mesh embedding has been used for viscous high Mach number flows. Several adaptation criteria have been tested to show that the optimal criterion depends upon the most relevant flow features to be resolved accurately.

Crucial characteristics of any mesh embedding technique are the adaptation criterion and the treatment of fluxes at boundaries of adaptation regions in order to maintain stability, conservation, and accuracy of the solution. Dealing with high-speed flows, the treatment of the interfaces between adapted regions must be particularly robust, in order to avoid instability of the solution if the embedded mesh boundaries are near high gradient regions.

The strategy adopted here relies on a higher order, conservative reconstruction of the coarse grid solution in those cells that lie just along the boundaries of embedded regions: this reconstruction is used to define auxiliary points needed by the numerical scheme for a correct evaluation of fluxes at boundaries of embedded regions. However, higher order reconstruction could induce oscillations or even instabilities. To inhibit such oscillations and/or instabilities, slope limiting is enforced in the reconstruction, so as to avoid the reconstructed values that lie outside the minimum and maximum of neighboring average cell values.

The reliability and usefulness of the technique is demonstrated by its application to shock-wave boundary-layer interaction problem[11] and to a variety of viscous high Mach number flows around a longitudinal section of a re-entry-type vehicle.

Governing Equations

The governing equations solved are the laminar compressible Navier-Stokes equations in conservation form

$$\frac{\mathrm{d}}{\mathrm{d}t}\int_S \boldsymbol{W}\,\mathrm{d}S = -\oint_{\partial S}(\boldsymbol{F}_E - \boldsymbol{F}_V)\cdot \underline{n}\,\mathrm{d}s \tag{1}$$

where $\boldsymbol{W}$, $\boldsymbol{F}_E$, $\boldsymbol{F}_V$ are, respectively, the vector unknown, the inviscid and viscous flux tensors, defined as follows:

$$\boldsymbol{W} = [\rho, \rho\underline{u}, \rho E]^T$$

$$\boldsymbol{F}_E = [\rho\underline{u}, \rho\underline{\underline{uu}} + p, \rho\underline{u}(E + p/\rho)]^T$$

$$\boldsymbol{F}_V = [0, \underline{\underline{\sigma}}, -(\underline{q} - \underline{u}\cdot\underline{\underline{\sigma}})]^T \tag{2}$$

and

$$\underline{\underline{\sigma}} = \mu(\nabla\underline{u} + \nabla\underline{u}^T) - \tfrac{2}{3}\mu\nabla\cdot\underline{u}\,\underline{\underline{U}} \tag{3}$$

$$\underline{q} = -\lambda\nabla T \tag{4}$$

$$\mu = \begin{cases} \mu_\infty \tilde{T} & \text{if} \quad \tilde{T} \le s_1 \\ s_1^{1/2}\mu_\infty \tilde{T}^{1/2}\dfrac{1 + s_2/s_1}{1 + s_2/\tilde{T}} & \text{if} \quad \tilde{T} > s_1 \end{cases} \tag{5}$$

where $\tilde{T} = T/T_\infty$; $s_1 = 120/T_\infty$; $s_2 = 110/T_\infty$; $\underline{\underline{U}}$ is the unit tensor; and λ is the thermal conductivity. The given set of governing equations is completed by the equation of state:

$$p = (\gamma - 1)\rho\left(E - \frac{\underline{u}\cdot\underline{u}}{2}\right) \tag{6}$$

Numerical Solution

The approach followed in the present work is based on a cell-centered finite volume time-marching formulation. The

---

Presented as Paper 91-0149 at the AIAA 29th Aerospace Sciences Meeting, Reno, NV, Jan. 7–10, 1991; received Feb. 5, 1991; revision received Nov. 22, 1991; accepted for publication Dec. 2, 1991.

* Associate Professor, Department of Mechanics and Aeronautics. Member AIAA.

† Graduate Student, Department of Mechanics and Aeronautics.

discretization of space and time is separated by use of the method of lines, thus reducing the system of discretized equations to a system of ordinary differential equations. The basic numerical algorithm employs symmetric discretization of both the inviscid and viscous terms. Time integration is performed by a five-stage Runge-Kutta technique.

It is well recognized that the topology of the grid is primarily responsible for the numerical errors on the solution of the conservation equations for compressible flows. Adequate resolution can be achieved only by using very fine grids. However, the need of accuracy contrasts with the need of high computational efficiency. It should be pointed out further that, in general, higher accuracy is needed not everywhere in the field, but only in the regions where "local" phenomena occur: across shocks, at the shock/boundary-layer interaction site, and so forth. Hence, to minimize both computational costs and numerical errors, a technique, which is capable of enhancing the accuracy only where needed, should be devised.

Adaptive mesh embedding is a good candidate. With such a technique, the grid is refined by embedding cells locally according to an adaptation criterion: each cell is subdivided both in x and y into four smaller cells whenever the criterion is met. All cells of embedded types are organized in a grid that, in the hierarchical sense, is of higher level (i.e., finer). Grids belonging to different levels are organized in a tree-like structure, and pointers are introduced for: 1) establishing grid communication across the different levels; 2) determining cell adjacency relationships; and 3) obtaining the position of embedded cell vertices for an efficient evaluation of the viscous contributions. At present, only two levels of embedding are allowed. Additional embedding would require more pointers to address efficiently more than two grid levels.

A solution vector is defined on each grid, and time stepping is performed separately on each one.[5-9] Let G_0 be the level ℓ-0 grid (the initial one), and G_1 and level ℓ-1 grid (the embedded one), then $\boldsymbol{W}_0$ and $\boldsymbol{W}_1$ indicate the corresponding solution vectors.

The solution is first obtained on the initial grid according to the following algorithm

$$\begin{aligned} \boldsymbol{W}_0^{(0)} &= \boldsymbol{W}_0^n \\ \boldsymbol{W}_0^{(k)} &= \boldsymbol{W}_0^{(0)} + a_k \frac{\Delta t_0}{S_0} \boldsymbol{R}(\boldsymbol{W}_0^{(0)}, \mathrm{W}_0^{(k-1)}) \\ \boldsymbol{W}_0^{n+1} &= \boldsymbol{W}_0^{(5)} \end{aligned} \tag{7}$$

where $\boldsymbol{R}$ is the residual defined as the sum of the inviscid ($\boldsymbol{R}_I$), viscous ($\boldsymbol{R}_V$) and adaptive dissipation ($\boldsymbol{R}_D$) contributions:

$$\boldsymbol{R} = \boldsymbol{R}_I^{(k)} + \boldsymbol{R}_V^{(0)} + \boldsymbol{R}_D^{(k)} \tag{8}$$

The coefficients of the Runge Kutta scheme that guarantee high frequency damping behavior[12] are set equal to: $a_1 = \frac{1}{4}$; $a_2 = \frac{1}{6}$; $a_3 = \frac{3}{8}$; $a_4 = \frac{1}{2}$; $a_5 = 1$. To ensure good parabolic stability, the adaptive dissipation contribution is evaluated only at odd stages according to the formula:

$$\boldsymbol{R}_D^{(2m+1)} = (1 - \beta_{2m+1})\boldsymbol{R}_D^{(2m-1)} + \beta_{2m+1}\boldsymbol{R}_D(\boldsymbol{W}_0^{(2m)}) \tag{9}$$

where $m = 1, 2$ and the values of the βs are: $\beta_1 = 1$; $\beta_2 = 0$; $\beta_3 = 0.56$; $\beta_4 = 0$; $\beta_5 = 0.44$. At even stages (the second and the fourth), the term $\boldsymbol{R}_D$ is evaluated as follows:

$$\boldsymbol{R}_D^{(2m)} = \boldsymbol{R}_D^{(2m-1)} \tag{10}$$

Numerical Inviscid Flux Contribution $\boldsymbol{R}_I$

The numerical inviscid flux contribution is evaluated according to the following formula

$$\boldsymbol{R}_I(\boldsymbol{W}_0) = \sum_{\beta=1,4} (\boldsymbol{F}_{E,\mathrm{num}} \cdot \underline{n})_\beta \Delta s_\beta \tag{11}$$

where β indicates the cell faces and the subscript num stands for numerical. At the midpoint of cell face $\beta = 1$ (defined as $(i + 1/2, j)$) $\boldsymbol{F}_{E,\mathrm{num}}$ is computed with a cell-centered approximation that ensures consistency and conservation:

$$(\boldsymbol{F}_{E,num} \cdot \underline{n})_{i+1/2,j} = \tfrac{1}{2}(\boldsymbol{F}_{Ei,j} + \boldsymbol{F}_{Ei+1,j}) \cdot \underline{n}_{i+1/2,j} \tag{12}$$

Numerical Viscous Flux Contribution ($\boldsymbol{R}_V$)

The numerical viscous flux contribution is cast in the following form:

$$\boldsymbol{R}_V(\boldsymbol{W}_0) = \sum_{\beta=1,4} (\boldsymbol{F}_{V,\mathrm{num}} \cdot \underline{n})_\beta \Delta s_\beta \tag{13}$$

According to the constitutive equations, the viscous fluxes depend upon the gradients of the primitive variables (velocity and temperature). The numerical counterpart is obtained by applying Gauss theorem to a computational cell (see Fig. 1) whose vertices are the two grid nodes I, J and $I, J - 1$, and the centers of the two adjacent cells i, j and $i + 1, j$. For an arbitrary function φ, the numerical derivatives at cell face $(i + \frac{1}{2}, j)$ are:

$$\left(\frac{\partial\varphi}{\partial x}\right)_{i+1/2,j} = \frac{\varphi_{EW}y_{NS} - \varphi_{NS}y_{EW}}{x_{EW}y_{NS} - x_{NS}y_{EW}}$$

$$\left(\frac{\partial\varphi}{\partial y}\right)_{i+1/2,j} = -\frac{\varphi_{EW}x_{NS} - \varphi_{NS}x_{EW}}{y_{EW}x_{NS} - y_{NS}x_{EW}}$$

where

$$\begin{aligned} \varphi_{EW} &= \varphi_{i+1,j} - \varphi_{i,j} \\ x_{NS} &= x_{I,J} - x_{I,J-1} \\ \varphi_{NS} &= \varphi_{I,J} - \varphi_{I,J-1} \\ x_{EW} &= x_{i+1,j} - x_{i,j} \end{aligned}$$

The cell vertex values $\varphi_{I,J}$, $\varphi_{I,J-1}$ are obtained by bilinear interpolation of cell center values. Hence, the discretized viscous flux contribution at cell face $\beta = 1$ is an algebraic function of grid and cell center values; that is

$$(\boldsymbol{F}_{V,\mathrm{num}})_{\beta=1} = g(\boldsymbol{W}_{0I,J}; \boldsymbol{W}_{0I,J-1}; \boldsymbol{W}_{0i,j}; \boldsymbol{W}_{0i+1,j}) \tag{14}$$

Adaptive Dissipation Flux Contribution ($\boldsymbol{R}_D$)

Adaptive dissipation is usually added for inviscid flow computations in order to prevent oscillations and even/odd point decoupling. Viscous high-speed flows are generally characterized by very steep gradients that may enhance the nonlinear effects. Consequently, the physical dissipation may not be

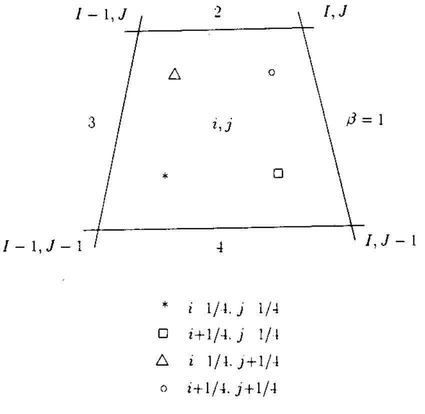

Fig. 1 Computational cell.

sufficient to damp the oscillations, and adaptive dissipation is still added. The latter contribution is defined as:

$$R_D(W_0) = \sum_{\beta=1,4} (F_{AD} \cdot \underline{n})_\beta \Delta s_\beta \tag{15}$$

The term F_{AD} represents the adaptive dissipation flux, which is a blending of first and third order derivatives, as proposed by Jameson et al.[13] For example, at cell face $\beta = 1$ one has

$$(F_{AD} \cdot \underline{n}\Delta s)_{i+1/2,j} = \lambda_{i+1/2,j}(\varepsilon^{(2)}_{i+1/2,j}\Delta^+_\zeta W_{i,j} - \varepsilon^{(4)}_{i+1/2,j}\Delta^+_\zeta \Delta^-_\zeta \Delta^+_\zeta W_{i,j}) \tag{16}$$

where ζ is the curvilinear coordinate associated with the "logical" i direction, and Δ^+ and Δ^- represent, respectively, the forward and backward difference operators. The variables $\lambda_{i+1/2,j}$, $\varepsilon^{(2)}_{i+1/2,j}$, and $\varepsilon^{(4)}_{i+1/2,j}$ are, respectively, the spectral radius of the inviscid flux jacobian, and the second and fourth-order pressure sensors, defined as

$$\varepsilon^{(2)}_{i+1/2,j} = k^{(2)} \max(\nu_{i-1}, \nu_i, \nu_{i+1}, \nu_{i+2})$$

$$\varepsilon^{(4)}_{i+1/2,j} = \max[0, (k^{(4)} - \varepsilon^{(2)}_{i+1/2,j})]$$

$$\nu_i = \frac{|p_{i+1,j} - 2p_{i,j} + p_{i-1,j} + \delta|}{|p_{i+1,j} + 2p_{i,j} + p_{i-1,j} + \delta|}$$

$$k^{(2)} = k^{(2)} \min(1, M^2)$$

where $k^{(4)} = 1/16$ and $\delta = 10^{-8}$ are constants. Observe that, in order to reduce the effects of artificial dissipation in the viscous layer, the constant multiplying the second-order pressure sensor has been scaled by the local Mach number.

The first term of Eq. (16) enforces an entropy-like condition and it prevents oscillations near shocks; the second term damps high-frequency modes and it affects the linear stability of the scheme.

Adaptive Mesh Embedding

The solution on the initial grid G_0 is obtained until quasi-convergence is reached: it is sufficient that the residual drops a few orders of magnitude. Then, a cumulative distribution function f is constructed, which represents the number of cells where an error indicator parameter ε is greater than a threshold value T. All cells, for which the adaptation criterion is met, are flagged, thus indicating that they are the ones where greater accuracy is required. Let N be the total number of such cells, then $4N$ embedded cells (of level ℓ-1 type) are generated by halving the N-flagged cells both in the x and y directions (see Fig. 1). The embedded grid G_1 is defined as the set of all ℓ-1-type cells. Higher level (finer) embedded grids are generated in a similar manner once the solution on the lower level ones has been obtained.

The topology of the "adapted" region (i.e., the region containing embedded cells) depends upon the selected adaptation criterion. Several criteria have been implemented

1) Criterion based on the gradient of a variable g

$$\varepsilon = \|\hat{\nabla} g\| \sqrt{S} \tag{17}$$

where $\hat{\nabla} g$ is the numerical gradient of g computed by use of Gauss theorem, and S is the cell area. The factor $\sqrt{S}$ is introduced to inhibit the refinement of the smallest ℓ-0-type cells.

2) Criterion based on the undivided difference of a variable g

$$\varepsilon = \|\Delta g\| = ((\Delta_i g)^2 + (\Delta_j g)^2)^{1/2} \tag{18}$$

where Δg is the undivided difference of g, and

$$\Delta_i g = g_{i+1,j} - g_{i-1,j}$$

$$\Delta_j g = g_{i,j+1} - g_{i,j-1}$$

This criterion is not affected by the metric (i.e., grid smoothness, aspect ratio distribution, etc.). However, it can generate finer and finer cells in those regions (such as across shocks) where the undivided difference remains constant independently of the mesh refinement.

3) Criterion based on the gradients of two variables g and q

$$\varepsilon = \|\hat{\nabla} g\| \cdot \|\hat{\nabla} q\| \tag{19}$$

Observe that, depending upon the selected criterion and the variables chosen for g and q, different adapted topologies arise. It has been shown[5] that for boundary-layer flows, stagnation regions, slip lines, and so forth, the most suited variable is the velocity. Vice versa, for shock-wave adaptation, the pressure is the most suited variable.

In the regions of adaptation, the multigrid strategy is exploited as a mean to improve the accuracy of the solution on the given initial grid G_0 as also pointed out by Brandt.[14] The computation proceeds from the finest to the coarsest embedded grid levels; and then the initial grid solution is updated. Thus, if m is the number of embedded grid levels, the solution is obtained in $m + 1$ phases. For example, assuming only one level of embedding, the strategy is as follows.

Initialization of W_1

Once G_1 is generated, the corresponding solution is initialized by means of a two-dimensional data reconstruction based on Legendre polynomials. To inhibit oscillations slope limiters are introduced, which enforce the constraint that no new maxima nor minima in the solution arise at centroids of embedded cells. Thus, second-order upwind approximation[5,6,15] of ℓ-1 variables at position $(i \pm \frac{1}{4}, j \pm \frac{1}{4})$ yields:

$$W_{1i\pm1/4,j\pm1/4} = W_{0i,j} \pm \tfrac{1}{8}(\phi^+\Delta_i^+ + \phi^-\Delta_i^-) \pm \tfrac{1}{8}(\phi^+\Delta_j^+ + \phi^-\Delta_j^-) \tag{20}$$

where

$$\Delta_i^\pm = \pm(W_{0i\pm1,j} - W_{0i,j})$$

$$\Delta_j^\pm = \pm(W_{0i,j\pm1} - W_{0i,j})$$

One-dimensional slope limited reconstruction yields:

$$\phi^\pm = \min(\phi_i^\pm, \phi_j^\pm)$$

where $\phi_i^\pm$, $\phi_j^\pm$ are, respectively, the slope limiters in the x and y directions. For example, given the one-dimensional zonewise averages of a variable u (see Fig. 2), second-order interpolation yields:

$$u_{i\pm1/4} = u_i \pm \tfrac{1}{8}(\Delta_i^+ + \Delta_i^-)$$

The enforcement of the constraints

$$u_{i+1/4} \leq u_{i+1} \qquad u_{i-1/4} \geq u_i$$

gives:

$$\phi_i^\pm = \operatorname{minmod}(\Delta_i^\pm, b\Delta_i^\mp)$$

where $b \leq 7$.

Likewise, slope-limited reconstruction in the j-direction yields:

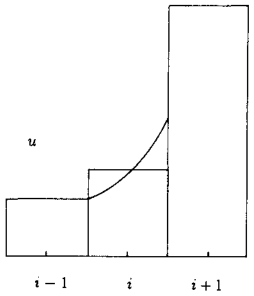

Fig. 2 One-dimensional slope limited reconstruction.

$$\phi_j^{\pm} = \text{minmod}(\Delta_j^{\pm}, b\Delta_j^{\mp})$$

Evolution of W_1

The solution on G_1 evolves according to Eq. (7):

$$W_1^{(0)} = W_1^n$$

$$W_1^{(k)} = W_1^{(0)} + a_k \frac{\Delta t_1}{S_1} R(W_1^{(0)}, W_1^{(k-1)})$$

$$W_1^{n+1} = W_1^{(5)}$$

Injection of W_1 on G_0

Once W_1 is computed, it is injected onto the underlying lower-level grid by means of volume weighted average, yielding:

$$W_{0i,j} = \frac{1}{S_{0,i,j}} [(\tilde{W}_1)_{i-1/4,j-1/4} + (\tilde{W}_1)_{i+1/4,j-1/4} + (\tilde{W}_1)_{i+1/4,j+1/4} + (\tilde{W}_1)_{i-1/4,j+1/4}] \tag{21}$$

where $\tilde{W} = S \cdot W$.

Evolution of W_0

A forcing function f is introduced to inhibit the loss of accuracy of W_0 in the adapted region. As in the multigrid approach, f is defined as:

$$f = \sum_{\ell-1} R_1^{n+1} - R_0^n \tag{22}$$

where the summation is extended to the ℓ-1 cells.

Then, in the adapted region, once the injection of W_1 and the construction of the forcing function are completed, the solution W_0 evolves as follows:

$$W_0^{(0)} = W_0^n$$

$$W_0^{(k)} = W_0^{(0)} + a_k \frac{\Delta t_0}{S_0} (f + R_0^{(k-1)})$$

$$W_0^{n+1} = W_0^{(5)} \tag{23}$$

In the region that does not contain embedded cells, the solution evolves according to Eq. (7).

Correction Transfer of W_0 on G_1

In the adapted region, the solutions W_0 and W_1 are advanced to the same time level by transferring the W_0 correction on G_1. A bilinear interpolation formula is used, that yields:

$$\begin{aligned} W_{1i-1/4,j-1/4} &= W_{1i-1/4,j-1/4} \\ &+ 0.5625(W_{0i,j}^{n+1} - W_{0i,j}^n) \\ &+ 0.1875(W_{0i-1,j}^{n+1} - W_{0i-1,j}^n) \\ &+ 0.1875(W_{0i,j-1}^{n+1} - W_{0i,j-1}^n) \\ &+ 0.0625(W_{0i-1,j-1}^{n+1} - W_{0i-1,j-1}^n) \end{aligned} \tag{24}$$

Interface Treatment

The interfaces, between grids of different levels, introduce internal boundaries that require a correct choice of boundary conditions to ensure conservation, accuracy, and stability. Allmaras and Baron[16] have defined interface fluxes by interpolation of coarse and fine grid fluxes, and have shown that stability can only be achieved at the expense of accuracy. Berger[8] and Berger and Jameson[9] have solved the problem by injecting fine embedded grid fluxes onto the coarse grid, and by introducing a fictitious layer of embedded cells, whose solution is determined by bilinear interpolation of the coarse grid one.

In the present work, conservation is enforced by injecting at each stage of the Runge Kutta algorithm the fine embedded grid fluxes onto the coarse grid. Moreover, a fictitious layer of embedded cells are introduced at the interfaces, where the boundary conditions are determined by interpolating coarse grid values by means of the formula used in the initialization step [Eq. (20)].

Results

In the present work, laminar high-speed flows have been computed. Two different test cases have been selected: a shock-wave boundary-layer interaction, and the flow over a double ellipse. The objective of the computations is twofold: 1) to study the effects of the grid quality; 2) and to show the dependency of the solution upon the topology of the adapted region.

Shock-Wave/Boundary-Layer Interaction

The first test case investigated is a laminar shock-wave boundary-layer interaction on a flat plate. The flow conditions correspond to those of Hakkinen et al.[11]: the freestream Mach number is $M_\infty = 2.0$; the impinging shock angle is $\theta = 32.6$ deg; the impinging shock location (measured from the leading edge) is $x_{shk} = 0.16$ ft; and the Reynolds number based on x_{shk} is $Re_{x_{shk}} = 0.296 \times 10^6$. The total length of the plate is about $1.2 \times x_{shk}$. The farfield boundary in the direction normal to the wall is about fifteen times the boundary-layer thickness, estimated immediately ahead of the shock impingement location. Freestream boundary conditions are imposed at inflow; at the farfield inviscid jump conditions for the given shock strength are set; no slip and adiabatic conditions are imposed along the wall; second-order extrapolation conditions are set at the outflow boundary.

This test case is simple and complex at the same time: it is simple because of the geometrical simplicity of the problem, and it is complex due to the presence of the shock wave impinging on the boundary layer. Depending on the strength of the shock and on the value of the freestream Mach number, the flow separates due to the interaction of the separation shock, which forms ahead of the impinging shock. The flow reattaches nearly at the foot of the reattachment shock, which arises behind the expansion zone occurring within the recirculation bubble.

The test case has been selected to study the effects of the grid quality on the solution when a mesh embedding technique is used, and to assess the computational efficiency of the proposed method. It must be observed that a laminar shock-wave boundary-layer interaction occurs mainly at the edge of the boundary layer. Consequently, an accurate resolution of the flow is required in the vicinity of the wall as well as in the proximity of the boundary-layer edge. Computations have been carried out on three different grids: 100 × 48; 150 × 72; and 200 × 96. Numerical experiments have indicated that the aspect ratio should assume values of $o(1)$ in the far field, and values of $o(10)$ in the vicinity of the wall, so as to capture both the leading-edge shock and the (impinging) shock-wave boundary-layer interaction. The grids have been generated in such a way to obtain an aspect ratio distribution that varies between 2 and 30, and are equally spaced in the x direction.

Embedded grids have been generated by using an adaptation criterion based on the product of pressure and velocity gradients, well suited for local refinement in the critical regions of the flow: near the leading edge; across the separation, impinging, and reattachment shocks; and near the boundary-layer edge where the interaction occurs. The threshold parameter has been selected in such a way to have an equal number of cells on the different grids. This refines at any grid level at most one-fourth of the total number of initial grid cells. A typical grid topology with two levels of embedding on the 150 × 72 mesh is shown in Fig. 3.

The wall pressure and skin friction distributions are shown in Figs. 4 and 5, where the results obtained on the 100 × 48 and 150 × 72 grids with two levels of embedding are compared vs the globally refined (200 × 96) grid solution and against the experimental values of Hakkinen. As the number of cells increases, a faster recompression across the separation shock followed by a slower recompression through the reattachment shock are predicted, in agreement with the experimental findings. The computed results also show that the reattachment shock is the most sensitive to grid refinement. For all cases, the extent of separation is predicted within a 10% error.

Let the percentage error ε on the computed plateau P pressure be defined as

$$\varepsilon = \left(\frac{p}{\tilde{p}}\right)_P - 1$$

where p and $\tilde{p}$ are, respectively, the computed pressure and the pressure estimated according to the following formula:[11]

$$\left(\frac{\tilde{p}}{p_\infty}\right)_P = 1 + \frac{\gamma M_\infty^2}{2} K \sqrt{\frac{2C_{f_\infty}}{\beta_\infty}}$$

where β, C_{f_∞}, and K are, respectively, the Prandtl-Glauert compressibility factor, the skin friction coefficient ahead of the interaction region, and a constant equal to 1.65.

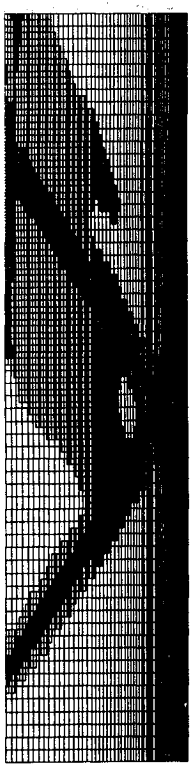

Fig. 3 Grid topology for 150 × 72 mesh with two levels of embedding.

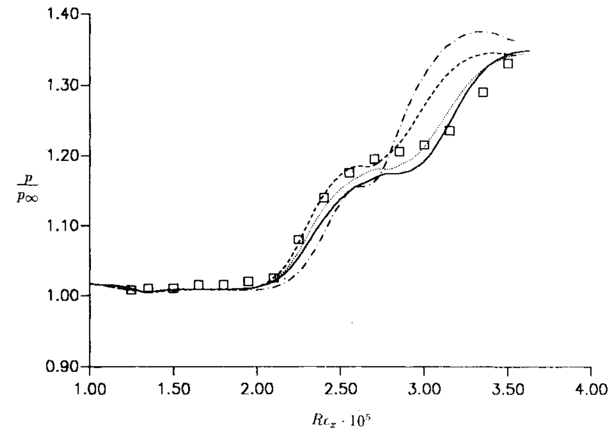

Fig. 4 Wall pressure vs Re_x for SWBLI (—·—, 100 × 48 ℓ-0; ---, 100 × 48 ℓ-2, ····, 150 × 72 ℓ-2; —, 200 × 96 ℓ-0; □, Ref. [11]).

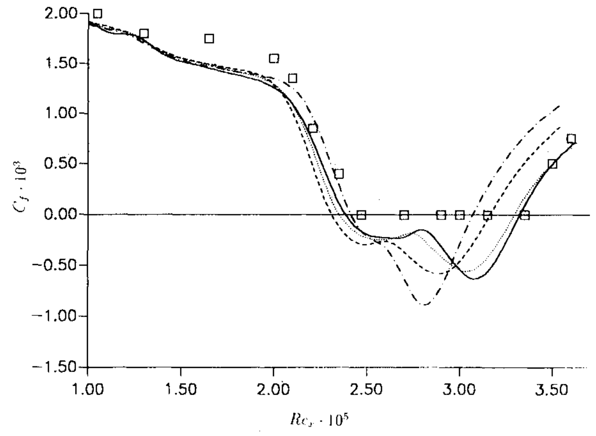

Fig. 5 Skin friction coefficient vs Re_x for SWBLI (—·—, 100 × 48 ℓ-0; ---, 100 × 48 ℓ-2; ····, 150 × 72 ℓ-2; —, 200 × 96 ℓ-0; □, Ref. 11).

The effects of grid refinement and adaptive embedding on ε are shown in Fig. 6, where the error is plotted vs the number of grid cells N (which include the embedded ones). The figure clearly shows that, by adaptive grid refinement, the plateau pressure is predicted with the same accuracy of a globally refined grid (the error variation is between 2 and 0.5%).

All computations have been performed on a IBM RISC-6000/530, and the total CPU time (in seconds) per unit cell for the different test cases is: 2.1 (ℓ-0) and 2.4 (ℓ-2) on the 100 × 48 grid; 3.4 (ℓ-0) and 3.5 (ℓ-2) on the 150 × 72 grid; and 7.1 on the 200 × 96 grid. Then, if one defines the efficiency E as the inverse of the ratio of the total CPU time per unit cell (of a given solution) to the total CPU time per unit cell of the reference solution (the globally refined one), for the same convergence level, E: 1) scales well with the number of initial grid cells; 2) and it does not depend strongly on the number of embedded grid levels.

Double Ellipse Test Case

The laminar flow over a double ellipse body has been investigated to show the dependency of the solution upon the topology of the adapted region, and to prove that an efficient "low-order" scheme does behave as a "high-order method," when used in conjunction with adaptive mesh embedding.

The geometry of the lower surface of the body is defined by:

$$\left(\frac{x}{0.06}\right)^2 + \left(\frac{y}{0.015}\right)^2 = 1$$

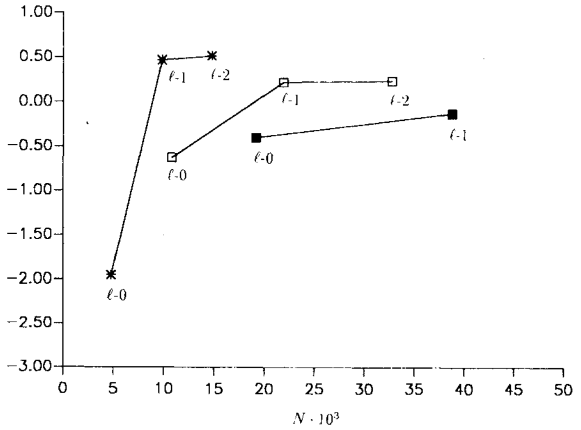

Fig. 6 Plateau pressure error vs number of cells (*, 100 × 48; □, 150 × 72; ■, 200 × 96).

For $x \leq -0.03$ the upper surface is described by the above formula; for $x > -0.03$ the curve describing the body is the following:

$$\left(\frac{x}{0.035}\right)^2 + \left(\frac{y}{0.025}\right)^2 = 1$$

The double ellipse is truncated at $x = 0$, and it is extended by a cylinder for $0 \leq x \leq 0.016$.

Several adaptation criteria have been tested for the different test cases. For all cases, only one level of embedding has been generated. Note that, for these test cases, the cells in the vicinity of the outflow boundary have not been refined. Such a limitation is not essential to assess the approach, because for hypersonic flows, the outflow boundary treatment can affect the solution only within the subsonic portion of the boundary layer.

All computations have been obtained on an initial grid consisting of 176 × 74 cells. Freestream conditions are imposed along the external (outermost) boundary, and second-order extrapolation conditions are imposed at the rightmost boundaries. At the wall, no-slip conditions and temperature are imposed.

The first test case corresponds to the following flow conditions: the freestream Mach number is $M_\infty = 8.15$; the angle of incidence is $\alpha = 0$ deg; the unit Reynolds number is $Re/m = 1.67 \cdot 10^7$; and the wall temperature is 288 K. The flow is characterized by a bow shock standing at a distance $\delta/c = 0.04$ ($c = 0.076$ m, the length of the body) from the nose, and a shock that originate at the canopy. The interaction of the two shocks affects the curvature of the bow shock. Moreover, the interaction of the canopy shock with the boundary layer causes the flow to separate with reattachment on the canopy. Due to the interaction, the canopy shock assumes the typical λ-shape.

The selection of the embedding criteria depends upon the physical phenomena that affect the details of the flows. For this test case, greater accuracy is required across the bow and the canopy shocks, and at the interaction site between the latter one with the boundary layer. Two criteria have been used: one based on the velocity gradient (FGU), and the other on the velocity and pressure gradients (FGUP).

For the same threshold parameter, the two criteria yield two different adapted regions. Near the wall it is the velocity variation, rather than the pressure one, responsible for the enrichment, and the embedded meshes generated by the two criteria do not differ from each other. Away from the wall, the criterion based on velocity and pressure gradients yields a better embedding across the canopy shock, and consequently a better definition of the latter.

The computed solutions are compared vs that obtained with a Runge-Kutta technique with adaptive dissipation without embedding (RKAD), and vs that computed with a total variation diminishing Runge-Kutta algorithm (RKTVD). The improvement in the resolution when using mesh embedding is evident. As observed from Figs. 7 and 8, where the pressure and skin friction coefficient distributions are reported, the details of the interaction between the canopy shock and the boundary layer can be detected with greater accuracy with mesh embedding.

RKAD predicts a small separation region: the flow separates at $x = -0.0375$ and reattaches at $x = -0.0263$. RKTVD yields a primary recirculation region followed by a secondary one: separation occurs at $x = -0.0381$ with reattachment at $x = -0.0261$. Two separations are also predicted with mesh embedding. The criterion based on velocity gradient predicts separation at $x = -0.0413$ and reattachment at $x = -0.0245$. The criterion based on velocity and pressure gradients predicts separation at $x = -0.0419$ and reattachment at $x = -0.0245$. A more accurate definition of the region of recirculation is obtained with the latter criterion.

The flow conditions for the second test case differ from those of the first case only in the angle of incidence (equal to 30 deg). The shock stand-off distance is $\delta/c = 0.069$. The differences with the case at zero incidence are mainly due to the large incidence, that causes the stagnation point to move forward along the lower surface. Moreover, the angle of attack determines a thinning of the shock layer on the windward side, with a thickening on the leeward side, and a weaker interaction between the canopy shock and the boundary layer.

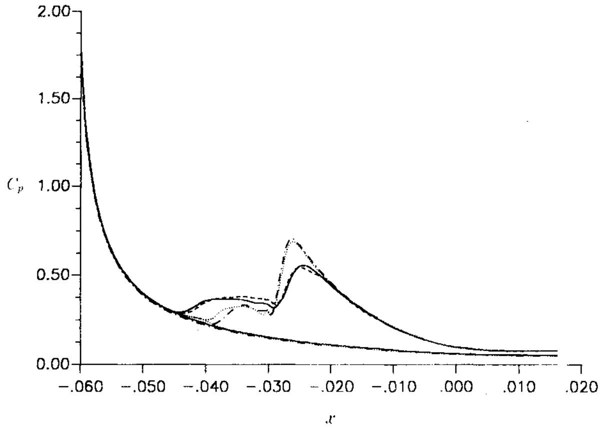

Fig. 7 Pressure coefficient vs x for $M_\infty = 8.15$, $\alpha = 0$ deg (—·—, RKAD; ····, RKTVD; ---, FGU; —, FGUP).

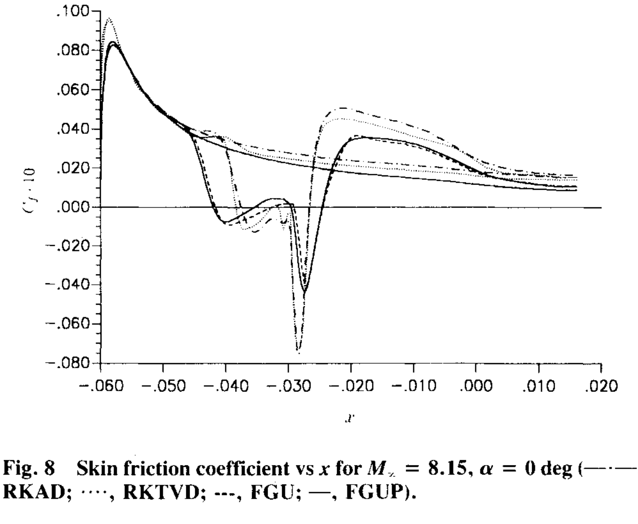

Fig. 8 Skin friction coefficient vs x for $M_\infty = 8.15$, $\alpha = 0$ deg (—·—, RKAD; ····, RKTVD; ---, FGU; —, FGUP).

The grids generated with the two criteria are shown in Figs. 9 and 10. The embedding criteria selected for this test case are based on the velocity gradient (FGU) and on the undivided difference of velocity (FDU). The latter criterion yields a smoother distribution of the embedded cells across the bow shock and in the vicinity of the canopy.

The computed iso-Mach lines are shown in Figs. 11–14; pressure and skin friction coefficients in Figs. 15 and 16. Comparison of the results with those obtained with RKAD and RKTVD indicates that the quality of the solution is greatly improved with just one level of embedding. The computations have been performed on an initial grid with the same number of cells as for the previous case. Hence, the grid is "finer" on the windward side (being that the shock layer is thinner) and "coarser" on the leeward side (where the shock layer is thicker). The solution with RKAD predicts, indeed, a rather smooth shock on the leeward side: an indication of poor resolution. RKAD predicts separation at $x = -0.0401$ and reattachment at $x = -0.0255$. Both RKTVD and the present method predict a larger extent of separation, with a primary and secondary recirculation. RKTVD predicts separation at $x = -0.0401$ and reattachment at $x = -0.0249$. The solutions obtained with the two different embedding criteria do not show appreciable differences (separation is at $x = -0.0405$ and reattachment at $x = -0.0250$). However, the criteria determine the topology of the adapted region and affect the computational efficiency. For the same threshold parameter, the first criterion yields fewer embedded cells and it is more efficient than the other one.

The technique has been applied to compute two more test cases corresponding to the following conditions: $M_\infty = 25$; $\alpha = 0$ deg, 30 deg; and $Re/m = 2.20 \cdot 10^4$; and the wall temperature is 1500 K. At such a high Mach number the flow is characterized by a thin shock layer and a thick viscous layer, and the shock-wave boundary-layer interaction is not as important as in the previous two cases. At zero incidence, the

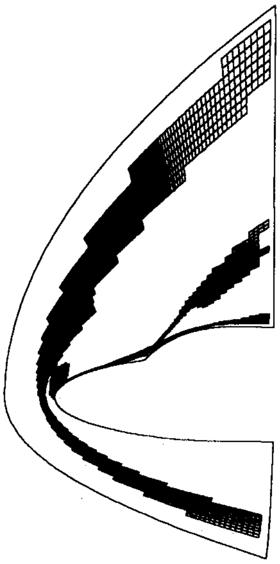

Fig. 9 Grid topology for $M_\infty = 8.15$, $\alpha = 30$ deg (FGU).

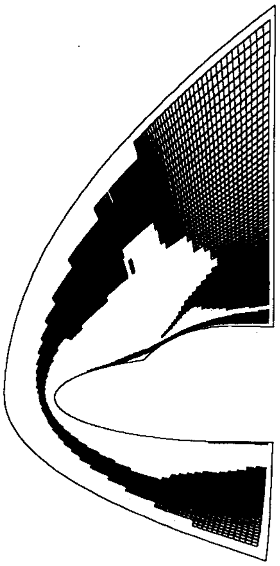

Fig. 10 Grid topology for $M_\infty = 8.15$, $\alpha = 30$ deg (FDU).

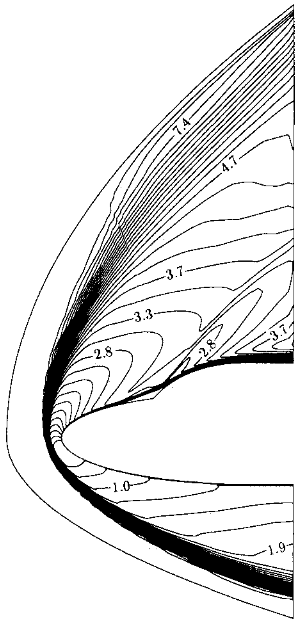

Fig. 11 Iso-Mach lines ($\Delta M = 0.25$) for $M_\infty = 8.15$, $\alpha = 30$ deg (RKAD).

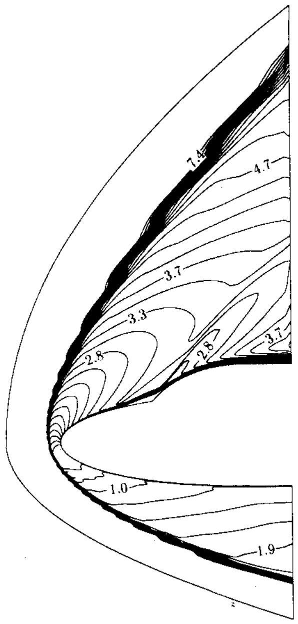

Fig. 12 Iso-Mach lines ($\Delta M = 0.25$) for $M_\infty = 8.15$, $\alpha = 30$ deg (RKTVD).

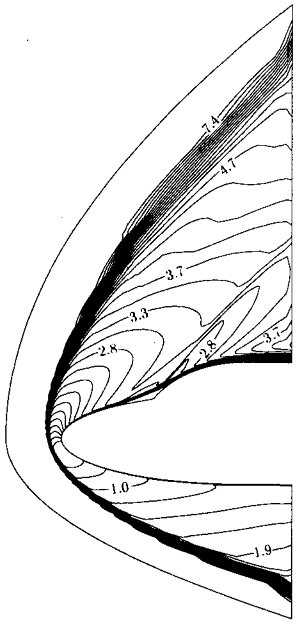

Fig. 13 Iso-Mach lines (ΔM = 0.25) for M_∞ = 8.15, α = 30 deg (FGU).

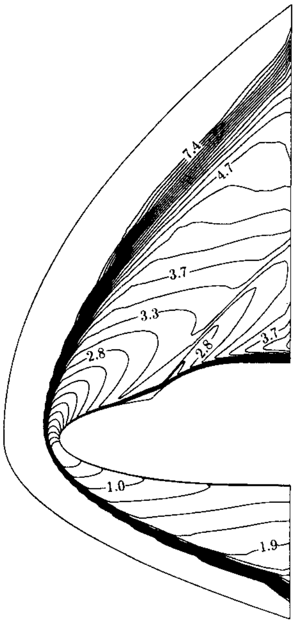

Fig. 14 Iso-Mach lines (ΔM = 0.25) for M_∞ = 8.15, α = 30 deg (FDU).

flow is characterized by the bow and canopy shocks and their mutual interaction. At 30 deg of incidence, the canopy shock is rather weak. Consequently, for a better shock resolution, the adaptation criteria must be defined via pressure sensors. In particular, at zero incidence, the selected criterion has been based on the pressure gradient (FGP); at 30 deg of incidence it has been based on the adaptive dissipation (FAD). Computations for the two cases have been carried out on a 176 × 74 (initial) highly stretched grid. The computed results show that the resolution of the shocks is greatly improved by mesh embedding. However, the solution does not show appreciable differences in the boundary layer, as observed from Fig. 17, where the skin friction coefficient of the 30 deg is plotted vs x/c.

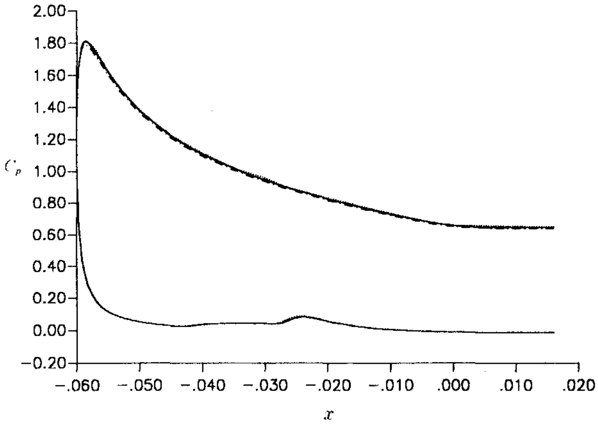

Fig. 15 Pressure coefficient vs x for M_∞ = 8.15, α = 30 deg (—·—, RKAD; ····, RKTVD; ---, FGU; —, FDU).

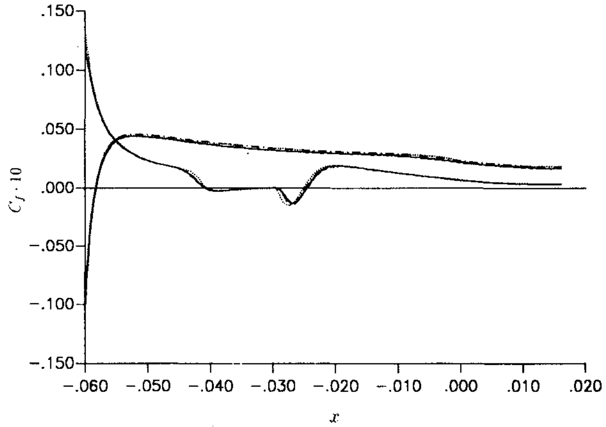

Fig. 16 Skin friction coefficient vs x for M_∞ = 8.15, α = 30 deg (—·—, RKAD; ····, RKTVD; ---, FGU; —, FDU).

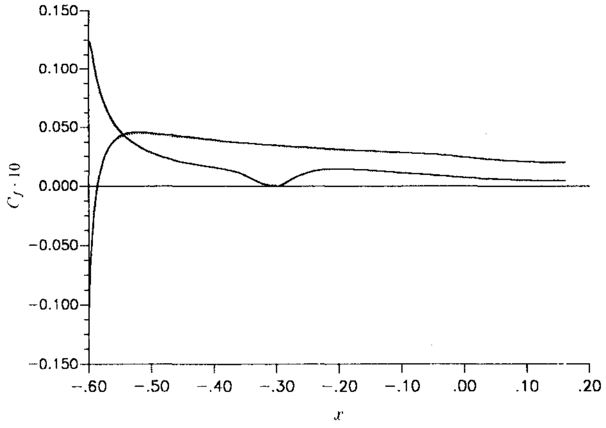

Fig. 17 Skin friction coefficient vs x for M_∞ = 25, α = 30 deg (—·—, RKAD; ····, RKTVD; —, FAD).

Conclusions

In the present work, a technique for improving the solution accuracy by adaptive mesh embedding has been applied to viscous high-speed flows.

The topology of the adapted region depends upon the adaptation criterion and it affects the quality of the solution. For a given problem, no general rules exist for selecting the most appropriate adaptation criterion. Only the knowledge of the physical phenomena of interest can give indications on the selection of the criteria. The computed results show that the solution accuracy of flows characterized by shocks and their mutual interactions can be improved by using criteria based on pressure sensors. If shock-wave/boundary-layer interaction phenomena are important, then the criteria must also depend upon a kinematic sensor.

The variety of the high-speed flows here computed, and the extensive comparison with two different methods (an efficient "low-order" one, and a low-efficiency, high-order technique) show that the adaptive mesh embedding technique here described is a powerful technique to increase the accuracy of low-order efficient schemes, and to make them behave as high-efficiency, high-order schemes.

References

[1] Hankey, W. L., and Holden, M. S., "Two-Dimensional Shock Wave-Boundary Layer Interactions in High Speed Flows," AGARDograph 203, 1975.

[2] Yee, H., "A Class of High-Resolution Explicit and Implicit Shock-Capturing Methods," NASA TM-101088, Feb. 1989.

[3] Bassi, F., Grasso, F., and Savini, M., "Finite Volume TVD Runge Kutta Scheme for Navier Stokes Computations," *Lecture Notes in Physics*, Springer Verlag, New York, Vol. 323, 1989, pp. 131–136.

[4] Barth, T. J., "On Unstructured Grids and Solvers," Von Karman Institute, Lecture Series 1990–03, March 1990.

[5] Grasso, F., "Numerical Solution of Viscous High Speed Flows," *Proceedings of the International Symposium on Computational Fluidynamics*, Japan Society of Computational Fluid Dynamics, Vol. 1, 1990, pp. 93–102.

[6] Bassi, F., Grasso, F., and Savini, M., "A Local Multigrid Strategy for Viscous Transonic Flows around Airfoils," *Lecture Notes on Numerical Fluid Mechanics*, Vieweg Verlag, Braunschweig, Vol. 20, 1988, pp. 17–24.

[7] Aftosmis, M. J., and Baron, J. R., "Adaptive Grid Embedding in Nonequilibrium Hypersonic Flows," AIAA Paper 89-1652, Buffalo, New York, June 1989.

[8] Berger, M. J., "Adaptive Finite Difference Methods in Fluid Dynamics," Von Karman Institute, Lecture Series 1987-04, March 1987.

[9] Berger, M. J., Jameson, A., "Automatic Adaptive Grid Refinement for the Euler Equations," *AIAA Journal*, Vol. 23, No. 4, 1985, pp. 561–568.

[10] Dannenhoffer J. F., III, and Baron, J. R., "Robust Grid Adaptation for Complex Transonic Flows," AIAA Paper 86-0495, Reno, Nevada, Jan. 1986.

[11] Hakkinen, R. J., Greber, I., Trilling, L., and Abarbanel, S. S., "The Interaction of an Oblique Shock Wave with a Laminar Boundary Layer," NASA Memorandum 2-18-59W, March 1959.

[12] Swanson, R. C., and Radespiel, R., "Cell Centered and Cell Vertex Multigrid Schemes for the Navier Stokes Equations," *AIAA Journal*, Vol. 29, No. 3, 1991, pp. 697–703.

[13] Jameson, A., Schmidt, W., and Turkel, E., "Numerical Solutions of the Euler Equations by Finite Volume Methods Using Runge-Kutta Time-Stepping Schemes," AIAA Paper 81-1259, Palo Alto, California, June 1981.

[14] Brandt, A., "Multilevel Adaptive Computations in Fluid Dynamics," *AIAA Journal*, Vol. 18, No. 10, 1980, pp. 1165–1172.

[15] Van Leer, B., "Upwind-Difference Methods for Aerodynamic Problems Governed by the Euler Equations," *Lectures in Applied Mechanics*, Vol. 22, 1985, pp. 327–335.

[16] Allmaras, S. R., and Baron, J. R., "Embedded Mesh Solution of the 2-D Euler Equations: Evaluation of Interface Formulations," AIAA Paper 86-0509, Reno, Nevada, Jan. 1986.